Supplementary Information

Light-Guiding Capillaries: A Robust Optofluidic Platform for Nanoparticle Tracking Analysis

Torsten Wieduwilt[1], Matthias Zeisberger[1], Walter Hauswald[1], Adrian Lorenz[1], Shayan Vazirieh Lenjani[2], Christian Rossner[2,3,4] and Markus A. Schmidt[1,5,6*]

[1]Leibniz Institute of Photonic Technology, Jena, Germany
[2]Leibniz Institute of Polymer Research Dresden, Dresden, Germany
[3]Faculty of Chemistry and Food Chemistry, Technische Universität Dresden, Dresden, Germany
[4]Department of Polymers, University of Chemistry and Technology Prague, Prague, Czech Republic
[5]Otto Schott Institute of Material Research, Friedrich Schiller University Jena, Jena, Germany
[6]Abbe Center of Photonics and Faculty of Physics, Friedrich Schiller University Jena, Jena, Germany
*markus-alexander.schmidt@uni-jena.de

Sec. 1 Brief description of alternative methods for determining the hydrodynamic diameter of NPs

In the following, alternative approaches for determining the hydrodynamic diameter of NPs are described and briefly placed into the context of NTA. These methods can be broadly divided into two groups, each exhibiting specific advantages and limitations in the context of NP analysis as outlined in the following:

- Methods that require fluorescent labeling: microfluidic diffusional sizing (MDS) [1], nanofluidic diffusional sizing (NDS) [2] and fluorescence correlation spectroscopy (FCS) [3]
- Label-free techniques: dynamic light scattering (DLS) [4], interferometric scattering microscopy (iSCAT) [5] and Taylor dispersion analysis (TDA) [6], [7]

Fluorescent labeling can introduce several limitations. The addition of a dye may alter the particle size and thereby influence the diffusion coefficient. It can also modify physicochemical properties such as surface charge, hydrophobicity or hydrophilicity, potentially affecting binding behavior and interactions. In addition, dyes may detach from the NP and diffuse freely in the medium, reducing the signal-to-noise ratio. Since not all particles can be readily labeled, specific surface functionalization strategies are often required. Another critical issue is photobleaching, which occurs when labeled particles remain in the focal volume for extended periods or are exposed to high excitation intensities. Photobleaching reduces signal intensity and limits measurement time, making long-term tracking of individual NP challenging, which is particularly relevant for FCS.

Furthermore, incomplete or non-uniform labeling (labeling efficiency) can lead to sample heterogeneity and artificial polydispersity.
Fluorescence-based methods are particularly suited for very small particles such as viruses, exosomes, lipid vesicles, DNA, RNA, proteins, and protein complexes and single organic molecules, which exhibit extremely small scattering cross-sections. MDS, for example, is widely used in protein analysis. It determines diffusion rates between two laminar liquid streams (analyte and buffer) in a microchannel, typically covering a size range of approximately 0.5 to 20 nm. Because protein samples are often highly polydisperse and consist of multicomponent mixtures, MDS has been further developed toward single-molecule detection (smMDS, single-molecule microfluidic diffusional sizing [8]).
Nanofluidic diffusional sizing (NDS) is also capable of single-molecule detection. In this method, the residence time of particles within nanofluidic cavities is measured to determine the hydrodynamic diameter. Fluorescence correlation spectroscopy (FCS) is based on the statistical analysis of fluorescence intensity fluctuations arising from dye-labeled particles diffusing through a very small excitation and observation volume. While highly sensitive, FCS requires a specialized confocal microscopy setup, high-sensitivity detectors, and precise optical alignment. The method becomes challenging for highly polydisperse samples.
Among the label-free techniques, dynamic light scattering (DLS) is the most widely used. It does not require fluorescent labeling and covers a broad size range from approximately 0.3 nm to 10 µm. However, DLS has well-known limitations when analyzing polydisperse samples and does not allow single-particle measurements, as a sufficiently high particle concentration - depending on the size and material of the particles, is required to generate an adequate scattering signal. Larger particles or aggregates can dominate the signal and distort the size distribution. Taylor dispersion analysis (TDA) is another label-free method. It measures the broadening of a small analyte pulse injected into a laminar flow within a capillary, where the concentration profile spreads due to axial convection and radial diffusion. TDA typically relies on ultraviolet light sources and UV absorption detection, restricting its applicability to UV-absorbing analytes. For non-absorbing species, such as certain polysaccharides or starches, more sensitive detection schemes such as refractive index detection or backscattering interferometry are required. TDA is generally applied to particles in the 0.1 to 400 nm range. Interpretation becomes more complex for particles outside this range or for aggregated samples.
Interferometric scattering microscopy (iSCAT) is a highly sensitive, label-free imaging technique that detects nanoscale objects by interfering light scattered from the specimen with a reference field. iSCAT typically requires high-power, highly coherent laser illumination and operation in mechanically stable, vibration-free, and thermally controlled environments. The method is very sensitive to mechanical drift and background noise, which can be challenging when targeting quantitative measurements.

Sec. 2 Derivation of modal loss

Within the context of the model represented by [9], the effective index of a mode in a liquid-filled capillary with an channel radius r_c much larger than the operation wavelength ($r_c \gg \lambda_0$) can be calculated as follows:

$$n_{\text{eff}} = n_{\text{liquid}} \left(1 - \frac{j^2}{2}\sigma^2 + i\frac{j^2}{2}\nu\sigma^3\right) \tag{1}$$

with the wavelength-dependent parameter $\sigma = \lambda_0/2\pi n_{\text{liquid}} r_{\text{c}}$ and the mode-dependent parameters ν and j. Here, ν characterizes the reflectivity of the single-interface boundary for glanzing light incidence, while j_{mn} stands for the n-th root of Bessel function J_{m}. For the TE, TM, HE and EH waves, ν and j can be calculated using the expressions

$$\nu = \begin{cases} \nu_{\text{TE}} &= 2/\sqrt{\epsilon - 1} \\ \nu_{\text{TM}} &= 2\epsilon/\sqrt{\epsilon - 1} \\ \nu_{\text{HE,EH}} &= (\nu_{\text{TE}} + \nu_{\text{TM}})/2 = (1+\epsilon)/(\sqrt{\epsilon - 1} \end{cases} \tag{2}$$

$$\text{and} \quad j = \begin{cases} j_{1,n} & : \text{TE}_{0n}, \text{TM}_{0n} \\ j_{m-1,n} & : \text{HE}_{mn} \\ j_{m+1,n} & : \text{EH}_{mn} \end{cases} \tag{3}$$

with parameter $\epsilon = (n_{\text{SiO}_2}/n_{\text{liquid}})^2$.
The numerical values of the zeros for the first order modes are listed in the following table.

Table S1: Numerical values of the zeros for the first order modes.

	$\mathbf{TE_{01}, TM_{01}}$	$\mathbf{HE_{11}}$	$\mathbf{EH_{11}}$	$\mathbf{HE_{12}}$	$\mathbf{EH_{12}}$	$\mathbf{HE_{21}}$	$\mathbf{EH_{21}}$
$\boldsymbol{j_{\text{m,n}}}$	$j_{1,1}$	$j_{0,1}$	$j_{2,1}$	$j_{0,2}$	$j_{2,2}$	$j_{1,1}$	$j_{3,1}$
zeros	3.832	2.405	5.136	5.520	8.417	3.832	6.380

The imaginary part of the modes can be obtained by inserting Eq. 2 and Eq. 3 in Eq. 1, leading to

$$\gamma \left[\frac{\text{dB}}{\text{cm}}\right] = \frac{54.57}{\lambda_0} \text{Im}\{n_{\text{eff}}\} = 0.11 \frac{\nu}{n_{\text{liquid}}^2} \frac{\lambda_0^2 j^2}{r_{\text{c}}^3} \tag{4}$$

with λ_0 and r_{c} given in centimeters.

Sec. 3 Theoretical background of nanoparticle tracking analysis

The key to understanding NTA lies in analyzing the diffusive motion of the individual NP of the ensemble which is a statistical process characterized by the diffusion coefficient D. Within NTA, this coefficient is determined by evaluating the temporal evolution of the position of the NP $x(t)$. The resulting mean square displacement (MSD) exhibits a linear dependence on the time interval Δt, following the relation:

$$MSD(i\Delta t) = \langle [x(t + i\Delta t) - x(t)]^2 \rangle = 2D\, i\Delta t \tag{5}$$

where $x(t)$ is the position of the particle at time t, Δt is the lag time (time interval between two recorded frames) and i the lag frame. $\langle\,\rangle$ indicates an expectation value. Experimentally, the expectation value is approximated by averaging over all measured displacements $(x_{i+\Delta i} - x_i)$ given by the measured trajectory, leading to [10], [11]

$$MSD(i\Delta t) \approx \frac{\sum_{j=0}^{N_{\text{f}}-i} (x_j - x_{j+i})^2}{N_{\text{f}} - 1} = 2D\, i\Delta t + (v \cdot i\Delta t)^2 + \sigma^2, \tag{6}$$

with the drift velocity v, that should be 0 at any time in the experiment, the number of frames N_f per trajectory and the localization accuracy σ^2, that introduces a positive offset in the MSD curve. The diffusion coefficient can then be determined from the slope (linear fitting) of the MSD curve. Using the Stokes–Einstein equation (Eq. 7), the hydrodynamic diameter d_h can then be calculated from the determined diffusion coefficient to

$$d_\mathrm{h} \approx \frac{k_\mathrm{B}T}{3\pi\eta D}, \tag{7}$$

where T is the absolute temperature, η is the dynamic viscosity of the ambient medium and k_B is the Boltzmann's constant. Note that the approximation in Eq. 6 becomes more accurate as the number of frames N_f per trajectory increases, thereby reducing the statistical error in determining the diffusion coefficient. The standard deviation of the diffusion coefficient D as a function of N_f can be calculated as follows [11]:
$\sigma_\mathrm{D} = D(2/1 - N_\mathrm{f})^{0.5}$

Sec. 4 Data processing/ Data analysis

Nanoparticle tracking: The image-based tracking of the nanospheres was carried out using the Python package Trackpy. This script has previously been applied to NTA experiments in various waveguide platforms and with different NP types, including gold, polystyrene, and biological particles such as viruses and phages [12], [13], [14], [15].

Data processing was performed in several steps:

(i) Preprocessing of the raw images (e.g., background removal, drift correction)

(ii) Localization of the NP by determining their center of mass in each frame.

(iii) Linking of trajectories and removal of short trajectories.

(iv) Determination of the diffusion coefficient for each nanoparticle via MSD analysis of the longitudinal (z-direction) part of the trajectories, including hindrance correction.

(v) Calculation of the hydrodynamic radius followed by z-score filtering.

Only the z-direction of the trajectories was used for diffusion analysis because free NP motion occurs along the longitudinal axis, whereas in the transverse direction diffusion is limited once the particle reaches the channel wall.

z-score filtering: The purpose of z-score filtering is to statistically identify and remove NPs that do not belong to the ultra-uniform NP ensemble. If a nanoparticle has a z-score above a defined threshold z_max, it is most likely an outlier (e.g., agglomerate, debris) and is excluded from the analysis. Here, a z_max value of 2.576 was applied, meaning that 1 % of the diameter values lie more than 2.576 standard deviations from the ensemble mean. Further details on z-score filtering are provided in Sec. S20 of the Supplementary Information of [14].

Impact of confinement on diffusion: When determining the hydrodynamic diameter of a NP moving in a microchannel, the influence of confinement on diffusion must be considered. Confinement affects diameter determination in two primary ways:

1. **Reduction of the MSD, particularly at longer observation times:** Due to the spatial restriction of transverse diffusion, as particles can contact the channel wall.

2. **Increased viscosity:** As a NP approaches the channel wall, fluid flow is more restricted, raising the local effective viscosity.

These effects are relevant only for transverse motion; longitudinal diffusion is influenced solely by the viscosity increase. Confinement can be corrected using the hindrance factor K_d, which relates the confined and free diffusion coefficients as $D_\mathrm{free} \approx D_\mathrm{confined}/K_\mathrm{d}$ and depends on the ratio of NP diameter d_p to channel diameter d_c [16], [17]. In the case of the polystyrene particles with $d_\mathrm{p} = 122\,\mathrm{nm}$ in a capillary with $d_\mathrm{c} = 20.2\,\mu\mathrm{m}$, $K_\mathrm{d} = 0.968$, which corresponds to an effect of $\approx 3.2\,\%$ on diffusion. For the 28 nm-gold particles in the 16 µm capillary, the effect is only $\approx 1.2\,\%$. Although this contribution is small, it was included in the evaluation of the hydrodynamic diameter.

Sec. 5 Optimization of parameters for reliable trajectory acquisition

Observation time: The observation time must exceed the diffusion time $t_\mathrm{D} = d_\mathrm{c}^2/(8D)$, which is required for a NP to diffuse from the capillary wall to the center. The reason for this is that the signal-to-noise ratio (SNR) decreases near the wall due to the reducing modal intensity of the guided mode. This increases the likelihood of localization errors and trajectory interruptions caused by NP loss in the tracking. Consequently, NPs diffusing near the glass wall typically show shorter trajectories than those located close to the center. If the observation time is longer than the diffusion time t_D, the particle has the possibility to diffuse from the wall to the center of the capillary.
For example, for a nanoparticle with $d_\mathrm{h} = 134\,\mathrm{nm}$, in a capillary with $d_\mathrm{c} = 20.2\,\mu\mathrm{m}$, $t_\mathrm{D} \approx 16\,\mathrm{s}$. In this case, a measurement duration of 25 s was chosen to ensure adequate observation time. To improve statistical reliability, several consecutive measurements were performed.

Frame rate: The frame rate must be adapted to the diffusive speed of the NP, as smaller NPs require higher temporal resolution. However, the maximum achievable frame rate is constrained by the camera's shutter speed, readout time, image dimensions, and required exposure time.
Note that for the experiments with the 15 nm-gold NPs, the frame rate was set to 200 fps accounting for the small scattering intensity, which required a longer exposure time (4.5 ms). In the other experiments, a frame rate of 400-450 fps could be used due to the shorter exposure times ($< 2\,\mathrm{ms}$). In all experiments the dimension of the image window was (4096×80) pixel.

Exposure time: This parameter strongly depends on the guided power inside the liquid channel, as well as on the scattering cross-section of the nano-objects. The exposure time should be chosen short enough to prevent saturation of the scattered signal and to ensure that motion blur is negligible. The latter means that no streaking artifacts from the moving objects should be visible. To meet this requirement, the average displacement $\bar{x} = (2Dt_\mathrm{exp})^{0.5}$ of the nanoparticle, during the exposure time (t_exp), must be less than the standard deviation of the Point spread function (PSF) of the microscopic imaging

system. Using the Gaussian approximation for the Airy disk ($\sigma_{\mathrm{PSF}} \approx 0.21\lambda/NA$), the maximum exposure time is given by:

$$t_{\mathrm{exp}} < \frac{0.022}{D}\left(\frac{\lambda}{NA}\right)^2 \tag{8}$$

where λ is the wavelength, NA is the numerical aperture of the microscopic objective, and D_{NP} is the diffusion coefficient of the nanoparticle. For a nanoparticle with a hydrodynamic diameter of 24.5 nm (see the experiments using 15 nm gold nanoparticles, Sec. 11 of the SI), the maximum exposure time is calculated to be 5.7 ms. As previously mentioned, an exposure time of 4.5 ms was selected for these experiments, which thus meets the above requirement.

Nanoparticle concentration: In addition to SNR, frame rate, and observation time, the trajectory length also depends on NP concentration. Excessively high concentrations can lead to intersecting trajectories, resulting in particle misidentification and shortened trajectories. Conversely, overly dilute solutions yield insufficient particle counts for meaningful statistical analysis. Thus, the NP concentration must be carefully adjusted to minimize trajectory overlap while ensuring sufficient data for achieving robust statistics.

Sec. 6 Mode beating inside the water-filled capillary

Slight periodic intensity modulations are observed in capillaries with a large channel diameter, caused by weak excitation of the HE_{12} higher-order mode and its interference with the fundamental mode (Fig. S1). This results from the mismatch between the Bessel-like mode profile of the capillary and the Gaussian mode of the delivery fiber. The presence of the HE_{12} mode was confirmed by comparing the measured beat length with simulation results: for a capillary with a channel diameter $d_{\mathrm{c}} = 24.8\,\mu\mathrm{m}$ (Fig. S1), the measured beat length is $L_{\mathrm{b}} = 1.3\,\mathrm{mm}$, in good agreement with the calculated value of $L_{\mathrm{b}} = 1.23\,\mathrm{mm}$ at $\lambda_0 = 532\,\mathrm{nm}$, based on the real parts of the effective indices $\mathrm{Re}\{n_{\mathrm{eff}}\}(\mathrm{HE}_{11}) = 1.3353$ and $\mathrm{Re}\{n_{\mathrm{eff}}\}(\mathrm{HE}_{12}) = 1.33487$. Note that in cases of non-ideal axisymmetric excitation, such as lateral misalignment of the delivery fiber, mode coupling between the fundamental mode and the HE_{21} mode may also occur.

Sec. 7 Orthogonal Alignment of the Sample Holder Relative to the Microscope Axis

For the Zemax-simulation mentioned in Sec. "2.3 applications" of the main text, a capillary and a 1-ARE fiber with a channel diameter of 16 µm and 25 µm were used. The larger diameter was chosen due to the reduced optical losses, lowering the required laser power and offering practical advantages, while the results remain valid for the microchannel sizes used in NTA experiments. Figure S2 shows the schematic used for the ray tracing simulations ((a) 1-ARE fiber, (b) capillary).
All surfaces, including the cover slip, are perfectly aligned orthogonally to the optical axis. The microscope is composed of an idealized paraxial $f = 18\,\mathrm{mm}$ objective lens and $f = 180\,\mathrm{mm}$ tubus lense. The magnification is $M = 10$. The positions of the NP in the transverse plane considered in the simulations are depicted by blue dots in Fig. S2(c).

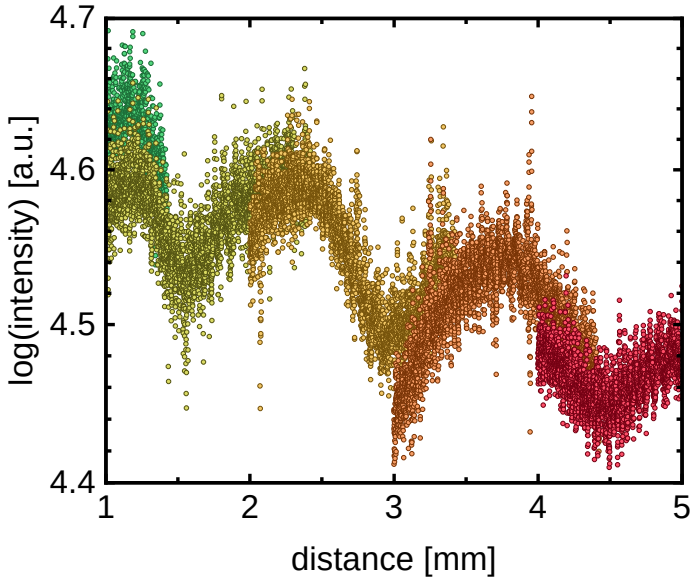

Fig. S1: Example of a periodic intensity distribution ($\lambda_0 = 532\,\mathrm{nm}$) measured along a 4 mm section of a water-filled capillary with a channel diameter of $d_c = 24.8\,\mu\mathrm{m}$. As discussed in the main text, the modulation results from mode coupling between the HE_{11} and HE_{12} modes.

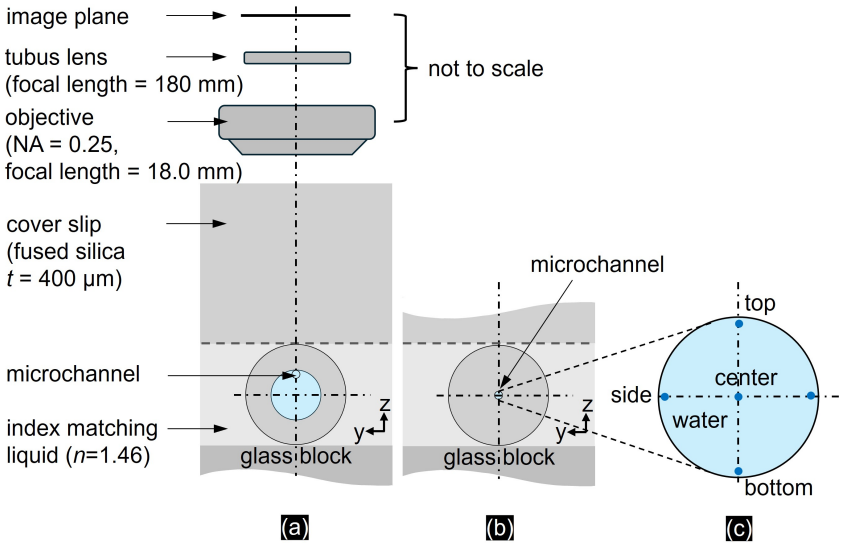

Fig. S2: Schematic of the microscope configuration used for the ray tracing simulations, showing the arrangement of components with details of dimensions and materials: (a) 1-ARE fiber, (b) capillary, (c) enlarged view of the water-filled channel – illustrates the simulated positions of the light-emitting NP, which are located 0.5 µm from the wall.

Sec. 8 Non-Orthogonal Alignment of the Sample Holder Relative to the Microscope Axis

In Section "2.3 applications" of the main text, simulations were conducted to reveal the imaging performance of the system assuming an idealized setup with the capillary and cover glass perfectly orthogonal to the microscope axis. To evaluate the effects of misalignment, we examine a capillary configuration where the glass block, housing both

the fiber and cover glass, is tilted at finite angles of 2.5° and 5° relative to the microscope axis (Fig. S3). These simulations focus on a capillary with an inner diameter of 16 µm.

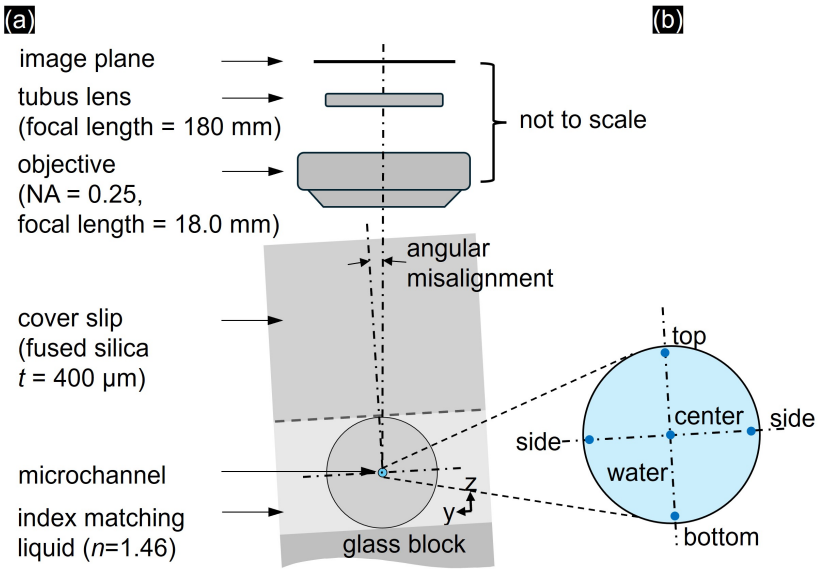

Fig. S3: Schematic of the microscope configuration used for ray tracing simulations, including angular misalignment: (a) Component arrangement, illustrating the tilt relative to the microscope axis. (b) Enlarged view of the water-filled capillary channel (16 µm inner diameter), highlighting the positions of light-emitting NPs. The positions near the capillary wall are 7.5 µm from the capillary axis.

The simulations (Fig. S4) reveal that angular misalignment (defined in Fig. S3) yields an asymmetrical point spread function and spot diagram. Comparable to the exactly aligned configuration, the largest RMS diameter occurs at the upper channel position (above the focal plane), with Figs. S4(a) and (d) demonstrating that a large fraction of rays extend beyond the Airy diameter, yielding RMS values approaching 26 µm. Figs. S4(a), (c) and (d) present the RMS values for NPs located 7.5 µm from the channel axis in a 16 µm capillary. As summarized in Tab. S2, image quality degrades with increasing angular misalignment for NPs near the channel wall - mirroring the trend observed in the simulations addressing the exactly aligned configuration.

Table S2: Ray trace results, showing the RMS-diameter values [µm] for the capillary after 10× magnification. The positions (x, y, z) [µm] indicated in the table header correspond to the positions shown in Fig. S3 for a channel diameter of 16 µm.

angular error	**top pos.** **(0, 0, 7.5)**	**center pos.** **(0, 0, 0)**	**side pos.** **(0, ±7.5, 0)**	**bottom pos.** **(0, 0, -7.5)**
0°	20.00	5.15	5.20	18.97
2.5°	21.11	8.65	8.67/8.51	20.30
5.0°	24.23	15.02	14.91/14.74	23.97

For a 25 µm capillary with a 2.5° misalignment, the RMS value reaches 33.15 µm for a particle positioned 12 µm above the channel axis. These results emphasize the critical role of precise optical alignment in reducing aberrations and preserving imaging performance. Diffraction-limited resolution is attained solely when all optical components, particularly

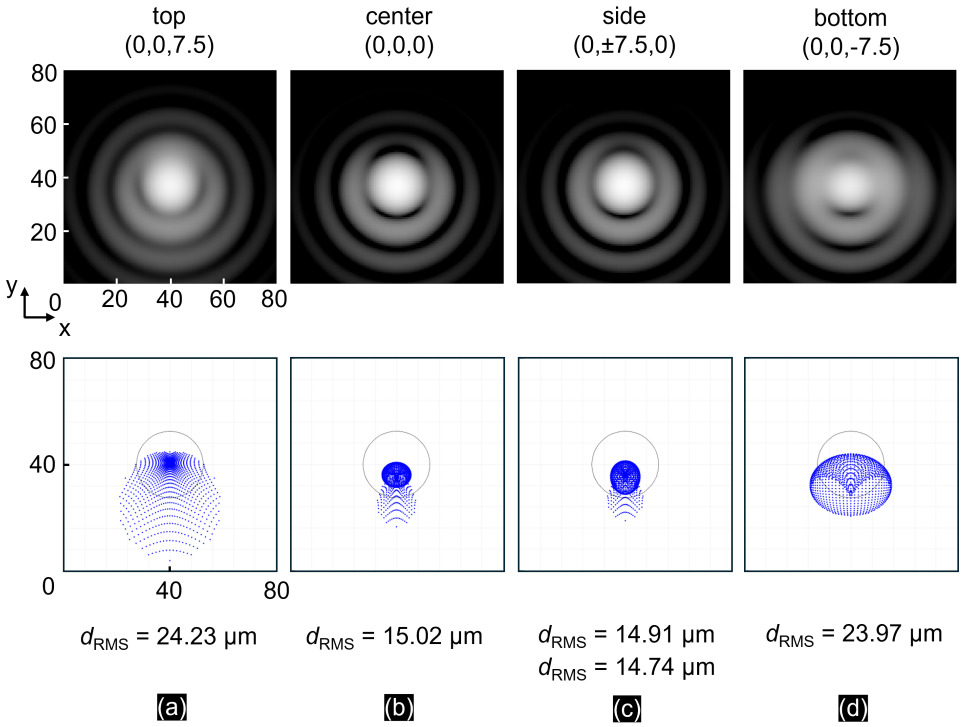

Fig. S4: Ray-tracing simulations of a 16 µm capillary with a 5° angular misalignment between the glass block (fiber and cover slip) and the microscope axis. The nanoparticle (NP) positions are: (a) top (7.5 µm above the channel axis), (b) center, (c) side (7.5 µm laterally offset from the channel axis), and (d) bottom (7.5 µm below the channel axis). Top row: PSF (log gray scale, representing 3 orders of magnitude), bottom row: corresponding spot diagram in the image plane ($M = 10$).

the cover slip interfacing the specimen and the microscope objective, are perfectly aligned. The following figure (Fig. S5) shows a selected image of light-scattering NPs recorded with our measurement setup. The observed Airy disks show slight asymmetry, indicating a small angular misalignment in the setup. However, this misalignment has a negligible impact on NP position determination, since the central peak intensity significantly exceeds that of the surrounding Airy rings (the image shown in Fig. S5 is highly saturated to visualize the Airy disks) enabling precise localization of the centroid of the diffusing NPs.

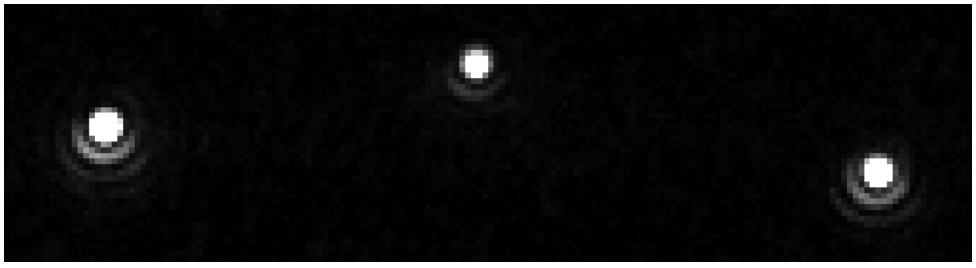

Fig. S5: Microscopic image of light scattered by three 28 nm gold NPs in a water-filled capillary (inner diameter 16 µm, image size: (170 × 45) pixel (59 × 15.5) µm). To enhance the visibility of the Airy disk, the scattering intensity was increased by a factor of 20 relative to the original image, resulting in saturation at the scattering center (image in linear gray scale).

Sec. 9 Capillary-based FaNTA experiments for characterizing NP mixtures

To demonstrate the capability of the system to analyze nanoparticle ensembles within a mixture, measurements were performed on a 1:1 mixture of polystyrene NPs with physical diameters of (100 ± 4) nm (Thermo Fisher Scientific Inc., cat. no. 3100A, $\mathrm{CV_{TEM}} = 7.7\,\%$) and (122 ± 3) nm (Thermo Fisher Scientific Inc., cat. no. 3125A, $\mathrm{CV_{TEM}} = 5.6\,\%$). Note that these are the same particle types (identical manufacturer specifications, differing only in batch number) that were used in one of our previous works (M. Nissen et al. [13]) to study the polydispersity of a two-species particle solution in a 1-ARE fiber. The results discussed below can therefore be directly compared to those reported in the work of M. Nissen et al. (see Tab. 3 in section "2.3 applications" of the main text). To verify that the individual NP solutions exhibit distinct single-peak hydrodynamic diameter distributions, an initial set of FaNTA experiments was performed on the monodisperse particle suspensions before mixing. The samples consisted of the particle solutions 3100A and 3125A diluted in ultrapure water containing 0.05 % Tween20 (nonionic surfactant). For each solution, eight consecutive measurements were conducted on two independent ensembles. Each measurement had a duration of 25 s at a frame rate of 400 fps, corresponding to 10,000 frames per measurement. The exposure time was 1.5 ms and a minimum trajectory length of 500 frames was applied within the MSD analysis. The results of these investigations, including the corresponding mean hydrodynamic diameters, are presented in Fig. S6, clearly showing single-peak diameter distributions.

The particle mixture was prepared such that approximately equal numbers of both particle types (about 20 nanoparticles of each size) were visible within the 4.56×10^{-7} ml observation volume of the 20.2 µm inner diameter capillary. For this purpose, the respective stock solutions (concentrations $c_{3125\mathrm{A}} = 1.816 \times 10^{13}$) NPs/ml and $c_{3100\mathrm{A}} = 1.0 \times 10^{13}$) NPs/ml were diluted using a 0.05 % Tween20 aqueous solution. The aqueous dilution solution was pre-filtered using a 20 nm pore filter (Whatman Anotop). To increase statistical accuracy, two independent particle ensembles were extracted from the sample solution and each characterized by eight individual measurements. The duration of a single measurement was 27.5 s at a frame rate of 400 fps, corresponding to 11,000 frames per measurement. The exposure time was 1.4 ms and the measurement temperature was 22.2 °C, monitored using a PT100 sensor positioned close to the capillary.

It should be noted that the CV values decrease with increasing minimum trajectory length. In our MSD analysis, a minimum trajectory length of 500 frames was applied. Shorter trajectories lead to a larger uncertainty in the diameter determination based on MSD analysis, resulting in a broader apparent diameter distribution. Consequently, a meaningful comparison of CV values is only possible under identical measurement and evaluation conditions, particularly with respect to frame rate and minimum trajectory length (see M. Nissen et al. [13]).

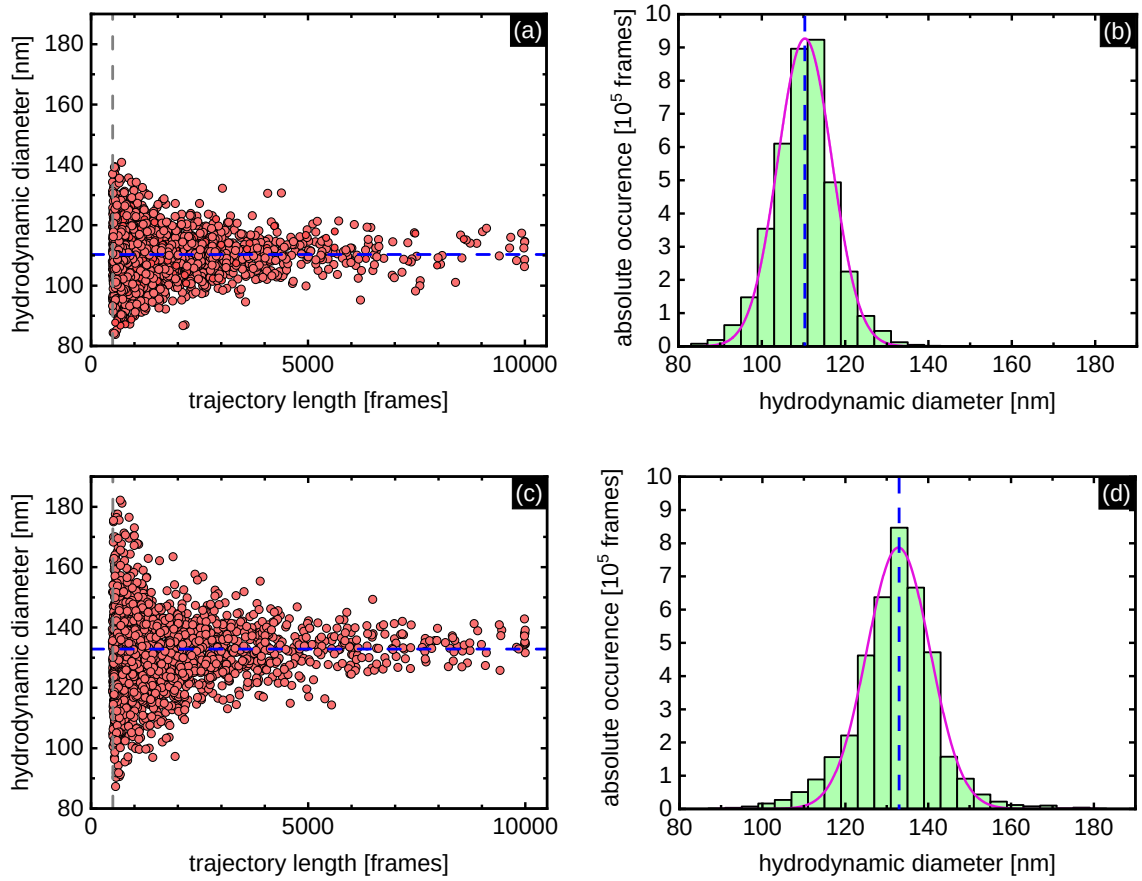

Fig. S6: FaNTA results for two monodisperse polystyrene NP samples (3100A: (a), (b); 3125A: (c), (d)), analyzed using a capillary with an inner diameter of 20.2 µm: (a) and (c) Hydrodynamic diameter as a function of trajectory length. (b) and (d) Corresponding trajectory-length-weighted histograms of the hydrodynamic diameter distribution, including a Gaussian fit (purple lines). In all four plots, the blue dashed lines indicate the mean hydrodynamic diameter of the respective distributions (sample 3100A: (110.3 ± 0.2) nm; sample 3125A: (132.8 ± 0.3) nm. In Figs. S6 (a) and (c) the vertical dashed gray line indicate the minimum number of frames considered.

Sec. 10 Capillary-based FaNTA experiments on cluster formation of P*N*iPAAm-functionalized gold NPs

To demonstrate the capabilities of the capillary-based system for detecting and quantifying changes in NPs, the formation of clusters of NPs functionalized with a stimulus-responsive polymer layer was investigated.

Nanoparticle system used: We employed functionalized gold NPs that exhibit a thermo-responsive clustering behavior. The used gold NP cores have a physical diameter of approximately 27 nm and are functionalized by poly(*N*-isopropylacrylamide) (PNiPAAm), which is a thermo-responsive polymer with a lower critical solution temperature (LCST) of about 32 °C at ambient pressure [18]. Its thermo-responsive behavior originates from the hydrophobic carbon backbone and side chains containing both a hydrophobic isopropyl group and a hydrophilic amide group in each monomer unit [19]. Upon changing the temperature, the NPs exhibit the following behavior:

- $\boldsymbol{T < \mathrm{LCST}}$: For temperatures below the LCST, hydrogen bonds form between water molecules and PNiPAAm, creating a hydrophilic environment (hydrated state) in which the polymer chains adopt an expanded coil conformation. This results in a larger hydrodynamic diameter of the functionalized NPs ($d_\mathrm{h} \approx 60\,\mathrm{nm}$). In this solvent-swollen state, the NPs are sterically stabilized by the polymer layer.

- $\boldsymbol{T > \mathrm{LCST}}$: For temperatures above the LCST, intra-molecular hydrogen bonding within PNiPAAm is favored, resulting in a more hydrophobic environment (dehydrated state). The polymer chains undergo a coil-to-globule transition, leading to a reduction in the hydrodynamic diameter of the NPs ($d_\mathrm{h} \approx 37\,\mathrm{nm}$). As the polymer shell collapses at $T \geq$ LCST, it no longer provides steric stabilization against aggregation. As a consequence, the colloidal particles may or may not aggregate depending on the extent of additional electrostatic stabilization, which can be modulated by electrolyte addition (surface charge screening) [20].

Synthesis of PNiPAAm-grafted gold nanoparticles: Citrate-caped quasi-spherical gold nanoparticles with an average diameter of $27 \pm 2.3\,\mathrm{nm}$ were synthesized according to a procedure described elsewhere [21]. An aqueous solution of these particles ($0.143\,\mathrm{mg/\,mL}$) was concentrated by centrifugation at relative centrifugal force (RCF) of 7000 for 1 hour at room temperature. After careful removal of the supernatant and re-dispersion in a minimum amount of water, the concentrated nanoparticle solution was added to a solution of thiol-terminated P*N*iPAAm ($M_\mathrm{n} = 30\,\mathrm{kg/\,mol}$, $Đ = M_\mathrm{w}/\,M_\mathrm{n} = 1.25$, Polymer Source Inc.) in water ($0.3\,\mathrm{mg/\,mL}$, corresponding to a target grafting density of $2\,\mathrm{chains/\,nm^2}$). The solution was incubated for 24 hours. In the next step, the sample was purified [22]from excess, non-grafted P*N*iPAAm molecules by three cycles of centrifugation/re-dispersion. First three cycles: centrifugation (6000 RCF, 1 hour), supernatant removal and re-dispersion in methanol; fourth cycle: centrifugation (6000 RCF, 1 hour), supernatant removal and re-dispersion in water.

Adaptation of the experimental setup: To demonstrate the temperature-sensitive effects experimentally, the setup was modified by integrating a single-stage Peltier element (15×15) mm. On top of the Peltier element, a 1 mm thick Borofloat glass substrate with an evaporated platinum resistance structure (PT1000) was mounted. The Pt structure was used to measure the temperature in close proximity to the fiber, which was positioned on the surface of the glass substrate. The fiber was covered with a 0.4 mm thick silica glass cover slip, and the space between the glass substrate and the cover slip was filled with immersion liquid - matched to the refractive index of silica, to avoid aberration.

Measurement of diameter change without clustering: To investigate the temperature dependence of the polymer shell, NP suspensions without the addition of electrolytes were characterized using capillary-based FaNTA. It is important to note that, since no electrolytes were added in these experiments, clustering did not occur and only the behavior of the polymer shell was probed [20],[23]. The resulting hydrodynamic diameter distributions at three selected temperatures Fig. S7 clearly shows a significant decrease in diameter when the temperature exceeds the LCST ($T >$ LCST) resulting from the mentioned shell collapse.

Characterization of nanoparticle clustering: To demonstrate clustering, the above-mentioned NPs were dispersed in a solution containing 100 mM NaCl and 0.5 mM NaOH. Our DLS measurements confirmed that a salt concentration of at least 25 mM NaCl is required to induce the clustering effect, in line with previous results [20], [24].

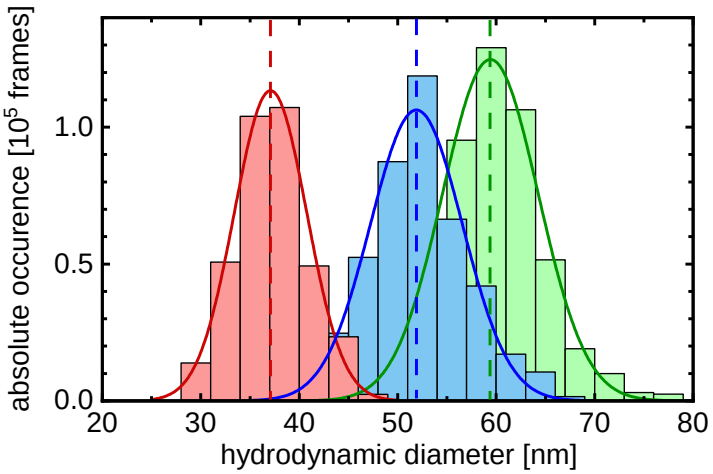

Fig. S7: Histograms of the hydrodynamic diameter distribution of PNiPAAm-functionalized gold NPs at three different temperatures (green: 20 °C, blue: 28 °C, red: 40 °C), measured using a capillary with an inner diameter of 20.2 µm. The colored lines indicate Gaussian fits to the data, with vertical dashed lines indicating the corresponding mean hydrodynamic diameter of the respective distributions (green: (59.4 ± 0.2) nm, blue: (51.9 ± 0.3) nm, red: (37.1 ± 0.1) nm).

In contrast to experiments performed in ultrapure water, particles in the NaCl solution exhibited partial adhesion to the inner wall of the capillary. This behavior can be attributed to electrostatic screening of the negatively charged citrate groups on the particle surface by Na^+ ions, as well as adsorption of Na^+ ions at the capillary wall. To mitigate this effect, the capillaries were pretreated by immersing them for about 3 hours in a ≈ 0.9 M KOH-solution, followed by thorough rinsing with ultrapure water. Here, the hydroxide ions in the KOH-solution promote deprotonation of silanol groups on the SiO_2 surface, thereby increasing the negative surface charge and reducing particle adhesion. In addition, a small amount of NaOH (0.5 M) was added to the particle solution to slightly shift the pH into the alkaline range ($\approx$ pH 8), further suppressing particle adhesion. It should also be noted that a significantly higher particle concentration was used in order to clearly observe the clustering effect.

Sec. 11 Capillary-based FaNTA experiments on 15 nm gold nanoparticles

In the Discussion section of the main text, the smallest detectable physical diameter of gold NPs using the capillary system was estimated to be 15 nm. To verify this estimate, we conducted NTA experiments on gold nanoparticles (Cytodiagnostics Inc.) of the same size. The gold particles are non-functionalized and are suspended in an aqueous sodium citrate solution (2 mM), which has been prefiltered using a 20 nm-pore-size filter (Whatman Anotop).

Unlike the particles manufactured by nanoComposix, these gold particles are not specified as ultra uniform. The CV value specified by the manufacturer is $\approx 12\,\%$, which, given an average hydrodynamic diameter of 24 nm, corresponds to a standard deviation in the diameter distribution of $\approx \pm 3$ nm. For the experiments, we used a capillary with an inner diameter of 25 µm to minimize losses ($\gamma \approx 2.6\,\frac{\mathrm{dB}}{\mathrm{cm}}$). Because the scattering cross-

section of a 15 nm gold particle is ≈ 60 times smaller than that of a 28 nm gold particle, we increased the laser power at the capillary input to approximately ≈ 120 mW and extended the exposure time to 4.6 ms. As a result, the frame rate was limited to 200 fps. Several measurements with a measuring time of 60 s (corresponding to 12000 frames) were conducted. For MSD analysis, a minimum trajectory length of 150 frames was applied. The results of these investigations are shown in Fig. S8.

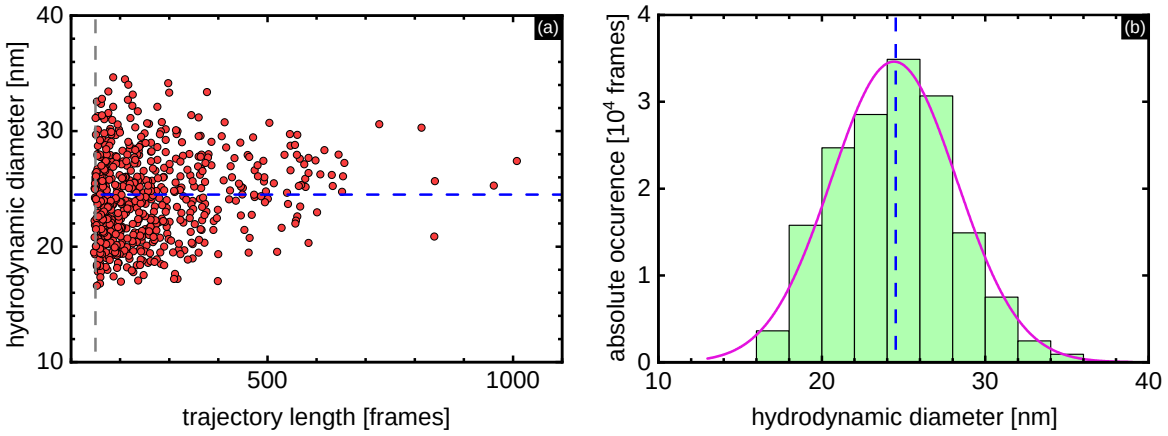

Fig. S8: Distribution of the hydrodynamic diameter for an ensemble of gold nanoparticles with an average physical diameter of 15 nm, measured using a capillary of 25 µm inner diameter. (a) Hydrodynamic diameter as a function of trajectory length for three consecutive measurements. The vertical gray dashed line indicates the minimum number of frames required for a trajectory to be included in the analysis. (b) Corresponding weighted histogram. In both plots, the blue dashed line marks the mean hydrodynamic diameter ((24.5 ± 0.5) nm).

As shown in Fig. S8, the determined hydrodynamic diameter of (24.5 ± 0.5) nm agrees very well with the manufacturer's specification of 24 nm (DLS measurement). The investigations thus confirm that the hydrodynamic diameter of gold NPs with a physical diameter in the range of 15 nm can be determined using a capillary.
However, based on the signal-to-noise-ratio (1:6-1:10) in these experiments, the investigations also showed that the lower detection limit is reached at a particle diameter of around 15 nm. For example, a 9 nm gold nanoparticle has a scattering cross-section that is 26 times smaller than that of a 15 nm gold nanoparticle.

Sec. 12 Upper limit on particle diameter (measurement range)

In general, the capillary-based FaNTA approach is suitable for measuring particles with diameters of up to several micrometers; however, several aspects must be carefully considered, including hydrodynamic hindrance effects due to confinement, gravitational sedimentation, changes in scattering behavior from Rayleigh to Mie regimes, and the resulting impact on localization accuracy and signal-to-noise ratio.

Impact of diameter ratio between particle and capillary: With increasing particle-to-capillary diameter ratio, diffusion within the capillary channel can no longer be regarded as completely free and unperturbed. As the NP approaches the capillary wall,

fluid displacement is restricted, leading to an effective increase in hydrodynamic drag, i.e. local viscosity. Consequently, MSD analysis results in an overestimation of the hydrodynamic diameter in these regions. This effect can be corrected by using the hindrance factor K_d, which represents an average correction over the channel radius and enables calculation of the corrected (free) diffusion coefficient via $D_\mathrm{free} = D_\mathrm{confined}/K_\mathrm{d}$. Fig. S9 shows the hindrance factor as a function of the NP/channel diameter ratio, calculated based on the model in [17].

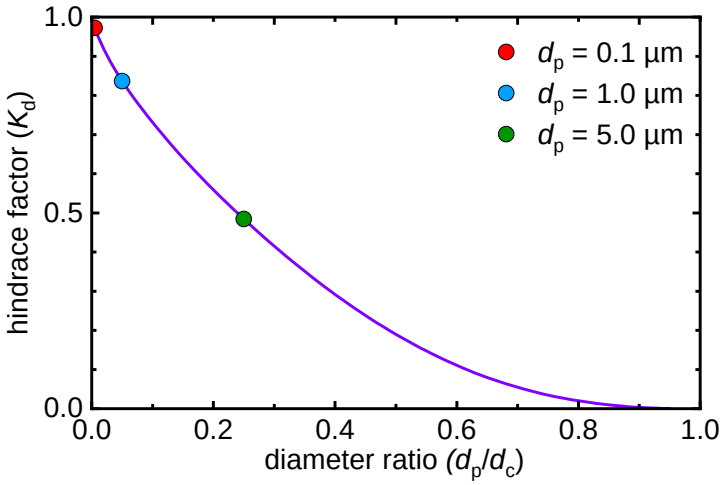

Fig. S9: Hindrance factor as a function of the diameter ratio between particle (d_P) and channel (d_c), calculated according to [17] for a channel diameter of 20 µm. The highlighted points represent different diffusion regimes (red: quasi-free diffusion; blue: moderately hindered diffusion; green: strongly hindered diffusion).

As shown in Fig. S9 for a channel diameter of 20 µm, the correction factor is $\approx 2.8\,\%$ for a 100 nm NP, $\approx 16.4\,\%$ for a 1 µm particle, and roughly $\approx 52\,\%$ for a 5 µm particle. Thus, with increasing diameter ratio, the magnitude of the correction increases and the associated uncertainty becomes more significant, making the analysis of larger particles increasingly critical.

Particle sedimentation due to gravitational forces: When investigating particles in the micrometer size range, it is important to consider that gravitational forces induce particle sedimentation, which superimposes Brownian motion. The corresponding settling velocity is proportional to the square of the particle diameter and to the density difference between the particle and the surrounding fluid [25]. Consequently, larger particles sediment faster than smaller ones, which, due to the confined volume of the capillary, can lead to the formation of a transverse concentration gradient across the channel cross-section.
To estimate the magnitude of this effect for the capillary configuration, Fig. S10 shows the simulated dependence of the settling velocity on particle size for different particle types (green: polystyrene, red: SiO_2, blue: gold) in water at a temperature of $T = 20\,^\circ\mathrm{C}$. The plot also includes the corresponding MSD (violet curve), which serves as an indicator of Brownian motion. When Brownian motion, i.e., the MSD, significantly exceeds the settling velocity at a given particle diameter, the particle remains in a stable suspended state; otherwise, it tends to sediment toward the bottom.
To experimentally demonstrate this effect, we introduced polystyrene microparticles (diameter 2 µm) into a capillary (channel diameter 25 µm) and observed clear sedimentation, i.e., settling of the particles at the bottom of the capillary within minutes.

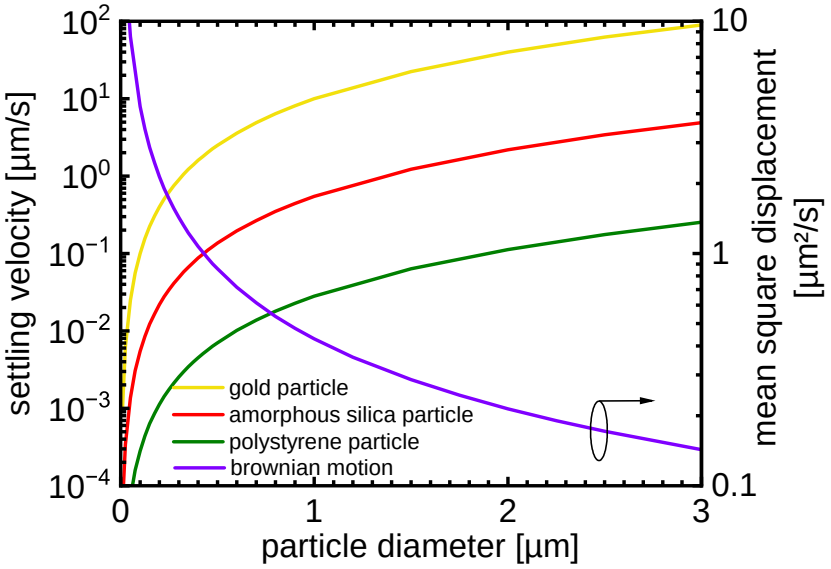

Fig. S10: Settling velocity and MSD of various micro- and nanoparticles diffusing in water as a function of particle diameter (using the Stokes' law [25] for a smooth sphere at steady-state conditions). Note that when Brownian motion significantly exceeds the settling velocity, the particle remains in a stable suspended state and does not undergo sedimentation.

Scattering mechanism (Rayleigh scattering vs. Mie scattering): Another important aspect is the fundamental difference in scattering behavior between nanoparticles and microparticles. Nanoparticles are much smaller than the wavelength of light and predominantly exhibit Rayleigh scattering, which increases strongly toward shorter wavelengths following the well-known λ^{-4} dependence. Their scattering is approximately isotropic, occurring uniformly in all directions. In contrast, microparticles have sizes comparable to or larger than the wavelength of the operating light and show Mie scattering, which mainly shows forward scattering in the direction of light propagation, making their detection in the context of FaNTA challenging, as detection is perpendicular to the fiber axis.

Microscopic imaging quality: Furthermore, high imaging quality of the particles in the recorded movies is essential to enable precise tracking of their trajectories. Our initial experimental investigations with 2 µm polystyrene particles have shown that the use of a 10×0.25 microscope objective, as employed for the measurements of nanoparticles, leads to a noticeable degradation of image quality for particles in this size range, making tracking and data analysis challenging.

References

[1] H. Xie, Y. Yang, C. Xia, T.-C. Lee, Q. Pu, Y. Lan and Y. Zhang, "Diffusional microfluidics for protein analysis", *Trends Analyt. Chem.* vol. 146, pp. 1-9, 2022

[2] R. P. B. Jacquat et al., "Single-Molecule Sizing through Nanocavity Confinement", *Nano Lett.* vol. 23, no. 5, pp. 1629-1636, 2023

[3] L. Yu., Y. Lei, Y. Ma, M. Liu, J. Zheng, D. Dan and P. Gao, "A Comprehensive Review of Fluorescence Correlation Spectroscopy", *Front. Phys.* vol. 9, pp. 1-21, 2021

[4] J. Stetefeld, S. A. McKenna and T. R. Patel, "Dynamic light scattering: a practical guide and applications in biomedical sciences", *Biophys. Rev.* vol. 8, no. 4, pp. 409-427, 2016

[5] N. S. Ginsberg, C.-L. Hsieh, P. Kukura, M. Piliarik and V. Sandoghdar, "Interferometric scattering microscopy", *Nat. Rev. Methods Primers*, vol. 5, no. 23, pp. 1-21, 2025

[6] M. R. Moser and C. A. Baker, "Taylor dispersion analysis in fused silica capillaries: a tutorial review", *Anal. Methods* vol. 13, no. 21, pp. 2357-2373, 2021

[7] J. Gouyon, A. Boudier, F. Barakat, A. Pallotta and I. Clarot, "Taylor dispersion analysis of metallic-based nanoparticles – A short review", *Electrophoresis* vol. 43, no. 23-24, pp. 2377-2391, 2022

[8] G. Krainer et al., "Single-molecule digital sizing of proteins in solution", *Nat. Commun.* vol. 15, no. 1, pp. 1-19, 2024

[9] M. Zeisberger and M. A. Schmidt, "Analytic model for the complex effective index of the leaky modes of tube-type anti-resonant hollow core fibers," *Sci. Rep.* vol. 7, no.1, pp. 11761(1-13), 2017

[10] X. Michalet, "Mean square displacement analysis of single-particle trajectories with localization error: Brownian motion in an isotropic medium," *Phys. Rev. E* vol. 82, no. 4, pp. 041914(1-13), 2010

[11] X. Michalet and A. J. Berglund, "Optimal diffusion coefficient estimation in single-particle tracking," *Phys. Rev. E* vol. 85, no. 6, pp. 061916(1-14), 2012

[12] R. Förster et al., "Tracking and Analyzing the Brownian Motion of Nano-objects Inside Hollow Core Fibers," *ACS Sensors* vol. 5, no. 3, pp. 879-886, 2020

[13] M. Nissen, R. Förster, T. Wieduwilt, A. Lorenz, S. Jiang, W. Hauswald and M. A. Schmidt, "Nanoparticle Tracking in Single-Antiresonant-Element Fiber for High-Precision Size Distribution Analysis of Mono- and Polydisperse Samples," *Small* vol. 18, no. 38, pp. 2202024(1-10), 2022

[14] T. Wieduwilt, R. Förster, M. Nissen, J. Kobelke and M. A. Schmidt, "Characterization of diffusing sub-10 nm nano-objects using single anti-resonant element optical fibers," *Nat. Commun.*, vol. 14, no. 1, pp. 3247(1-7), 2023

[15] D. Pereira, T. Wieduwilt, W. Hauswald, M. Zeisberger, M. S. Ferreira and M. A. Schmidt, "3D nanoprinted fiber-interfaced hollow-core waveguides for high-accuracy nanoparticle tracking analysis," *Light Sci. Appl.* vol. 14, no. 197, pp. 2-11, 2025

[16] J. M. Nitsche and G. Balgi, "Hindered Brownian Diffusion of Spherical Solutes within Circular Cylindrical Pores," *Ind. Eng. Chem. Res.* vol. 33, no. 9, pp. 2242-2247, 1994

[17] P. Dechadilok and M. Deen, "Hindrance Factors for Diffusion and Convection in Pores," *Ind. Eng. Chem. Res.* vol. 45, no. 21, pp. 6953-6959, 2006

[18] B. Ebeling, S. Eggers, M. Hendrich, A. Nitschke and P. Vana, "Flipping the Pressure- and Temperature-Dependent Cloud-Point Behavior in the Cononsolvency System of Poly(*N*-isopropylacrylamide) in Water and Ethanol", *Macromolecules* vol. 47, no. 4, pp. 1462-1469, 2014

[19] C. M. Papadakis, B.-J. Niebuur and A. Schulte, "Thermoresponsive Polymers under Pressure with a Focus on Poly(*N*-isopropylacrylamide) (PNIPAM)", *Langmuir* vol. 40, no. 10, pp. 1-20, 2024

[20] V. A. Turek, S. Cormier, B. Sierra-Martin, U. F. Keyser, T. Ding and J. J. Baumberg, "The Crucial Role of Charge in Thermoresponsive-Polymer-Assisted Reversible Dis/Assembly of Gold Nanoparticles", *Adv. Opt. Mater.* vol. 6, no. 8, pp. 1-6, 2018

[21] N. G. Bastús, J. Comenge and V. Puntes, "Kinetically Controlled Seeded Growth Synthesis of Citrate-Stabilized Gold Nanoparticles of up to 200 nm: Size Focusing versus Ostwald Ripening", *Langmuir* vol. 27, no. 17, pp. 11098-11105, 2011

[22] S. T. Jones, Z. Walsh-Korb, S. J. Barrow, S. L. Henderson, J. del Barrio and O. A. Scherman, "The Importance of Excess Poly(*N*-isopropylacrylamide) for the Aggregation of Poly(*N*-isopropylacrylamide)-Coated Gold Nanoparticles", *ACS* vol. 10, no. 3, pp. 3158-3165, 2016

[23] C. Rossner, I. Letofsky-Papst, A. Fery, A. Lederer and G. Kothleitner, "Thermoreversible Surface Polymer Patches: A Cryogenic Transmission Electron Microscopy Investigation", *Langmuir* vol. 34, no. 29, pp. 8622-8628, 2018

[24] S. Yusa, K. Fukuda, T. Yamamoto, Y. Iwasaki, A. Watanabe, K. Akiyoshi and Y. Morishima, "Salt Effect on the Heat-Induced Association Behavior of Gold Nanoparticles Coated with Poly(*N*-isopropylacrylamide) Prepared via Reversible Addition-Fragmentation Chain Transfer (RAFT) Radical Polymerization", *Langmuir* vol. 23, no. 26, pp. 12842-12848, 2007

[25] "Stokes' law", *Free Wikipedia* `https://en.wikipedia.org/wiki/Stokes'_law`